

The Nyquist soliton Kerr comb

Xiaoxiao Xue¹, Bofan Yang, Mian Wang, Shangyuan Li, Xiaoping Zheng², and Bingkun Zhou

Department of Electronic Engineering, Beijing National Research Center for Information Science and Technology, Tsinghua University, Beijing 100084, China

xuexx@tsinghua.edu.cn; xpzheng@tsinghua.edu.cn

Abstract

Dissipative Kerr cavity solitons (DKSs) are localized particle-like wave packets that have attracted people's great interests in the past decades. Besides being an excellent candidate for studying nonlinear physics, DKSs can also enable the generation of broadband frequency combs which have revolutionized a wide range of applications. The formation of DKSs are generally explained by a double balance mechanism. The group velocity dispersion is balanced by the Kerr effect; and the cavity loss is compensated by the parametric gain. Here, we show that DKSs can emerge through the interplay between dispersive loss and Kerr gain, without the participation of group velocity dispersion. By incorporating rectangular gate spectral filtering in a zero-dispersion coherently driven Kerr cavity, we demonstrate the generation of Nyquist-pulse-like solitons with unprecedented ultra-flat spectra in the frequency domain. The discovery of pure dissipation enabled solitons reveals new insights into the cavity soliton dynamics, and provides a useful tool for spectral tailoring of Kerr frequency combs.

Coherently driven dissipative temporal cavity solitons (DKSs), which were first demonstrated in a fiber ring cavity [1], are now being investigated intensely for their great potential in broadband optical frequency comb generation [2], [3]. With integrated miniature microcavities, soliton microcombs with ultra-compact volume and low power consumption have been demonstrated [4], [5], which may revolutionize a wide range of applications from high-precision metrology to large-capacity communications [6]-[14]. The formation of DKSs relies on an elegant balance of group velocity dispersion and Kerr effect as well as dissipative loss and parametric gain [2]. Depending on the sign of dispersion, DKSs with a rich diversity have been observed. In the anomalous dispersion region, the DKSs show similar temporal and spectral features to the classical solitons in optical fibers [1], [15]. In the normal dispersion region, rather different DKSs such as dark pulses and flat-top platicons may exist [16], [17]. To tailor the comb spectrum, most efforts to date have been focused on global dispersion engineering and mode crossing management [18]-[20]. Nevertheless, it has been found that the frequency dependence of cavity loss may also affect the comb generation. Spectral filtering induced modulational instability [21], [22] and pulse mode-locking [23], [24] akin to that in normal-dispersion mode-locked lasers have been reported. Despite the intense studies, the physics of DKSs is still far from being thoroughly explored and fully understood.

For applications such as spectroscopy [6], wavelength-division multiplexed communication [7], lidar ranging [8], [9], photonic neural computing [11], [12], microwave photonic signal processing [13], [14], etc., the frequency comb should ideally have a rectangular spectrum with uniform lines in a designed bandwidth. When the comb line phases are identical, the optical time-domain waveform can be described by a *sinc* function which is

usually called Nyquist pulse in high-speed communications [25]. However, it has been very challenging to achieve such a high spectral quality for Kerr combs to date. In this article, we demonstrate direct generation of Nyquist-pulse-like DKs by pumping a fiber ring Kerr cavity with programmable dispersion and loss. Surprisingly, the Nyquist soliton can be fully stabilized by dissipative loss and Kerr gain when group velocity dispersion is absent. The pure dissipation enabled solitons are related to interlocked switching waves and can be obtained in a deterministic way with pulsed pumping. The soliton transition dynamics is accurately captured by high-resolution intensity cross correlation. Our findings may be related to the Nyquist mode-locked lasers [26]-[28], and provide new insights into the soliton dynamics in zero-dispersion Kerr cavities [29], [30].

Formation dynamics of Nyquist soliton

Figure 1 shows an illustration of Nyquist soliton formation in a coherently driven Kerr cavity. The group velocity dispersion is assumed zero. The cavity is only transparent in a limited frequency range with an increased roundtrip loss outside the passband. The loss may be introduced by optical scattering and absorption in the cavity (i.e., intrinsic loss) or by a specially designed frequency selective coupler between the cavity and the external waveguide [31]. Under proper pump power and frequency detuning, a Nyquist pulse can be sustained in the cavity and an ultra-flat frequency comb is extracted in the outer waveguide. Since the group velocity dispersion is absent, only the dispersive loss and Kerr nonlinearity are responsible for the pulse shaping. The soliton is thus purely “dissipative” and distinct from previously reported cavity solitons for which the group velocity dispersion plays a critical role [2].

To reveal the formation dynamics of Nyquist solitons, numerical simulations are performed based on a normalized Lugiato–Lefever equation modified to take into account the dispersive loss (Supplementary Section 1.1). The results are shown in Figure 2. The Kerr cavity is pumped by a single-frequency continuous-wave laser. The initial intracavity field contains two well separated steps (usually named as switching waves, fronts, or domain walls in the literature [32]) that connect the two homogeneous solutions of the nonlinear equation. The switching waves keep still with respect to the fast time frame when there is neither group velocity dispersion nor frequency-dependent loss. A rectangular gate spectral filter with a bandwidth of 101 modes and null phase is then applied per roundtrip from the propagation distance of 50. The filtering effect introduces an energy exchange between the two step levels, causing the switching waves to move. The high plateau shrinks; and the two switching waves finally meet each other and get interlocked after the distance of 300. A stable Nyquist pulse is formed. The transient waveform and spectrum are shown in Figure 2b and 2c. A theoretical *sinc* pulse with its upper and lower bounds connecting the two homogeneous solutions (Supplementary Section 1.3), is also shown in Figure 2b. A good agreement between the numerical result and the theoretical estimation can be observed. The spectrum of the soliton is very close to a rectangle, with a power variation of only 2.9 dB within the filter passband.

In other simulations with different parameters, the switching waves may move in an opposite way causing the higher plateau to expand (Supplementary Section 1.4). Dark Nyquist pulse can be formed when the switching waves meet each other. It is found that once the switching waves are interlocked, the soliton can be maintained in a certain pump power and

detuning range. The locking dynamics shows multiple stabilities. Bright and dark solitons may coexist with the same set of parameters. Soliton hysteresis versus pump power and detuning is observed in simulations (Supplementary Section 1.5). Moreover, solitons can also be generated with filter shapes other than a rectangular gate. Supplementary Section 1.6 shows the results when the filter passband is given by Gaussian function of different orders. With the filter getting close to a rectangle, the soliton gets more like a Nyquist pulse.

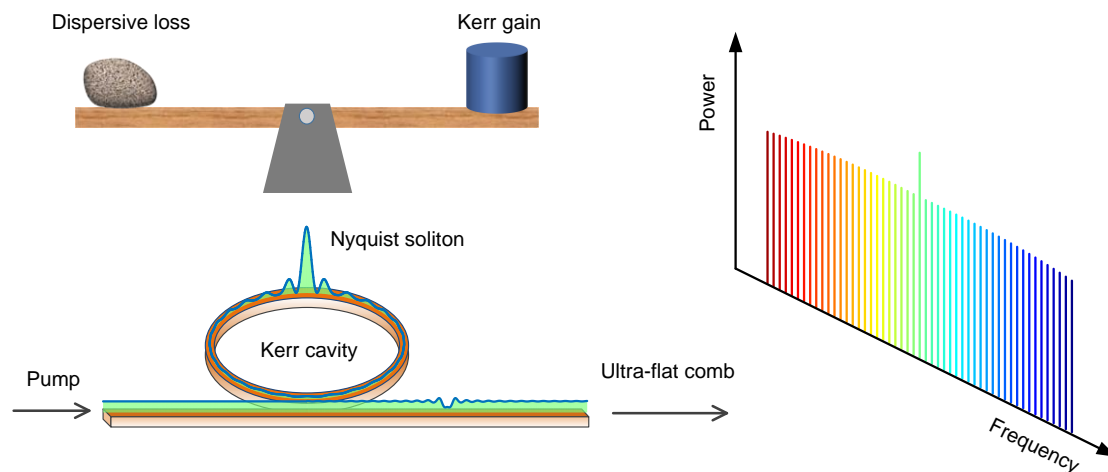


Figure 1 | Illustration of the Nyquist soliton Kerr comb.

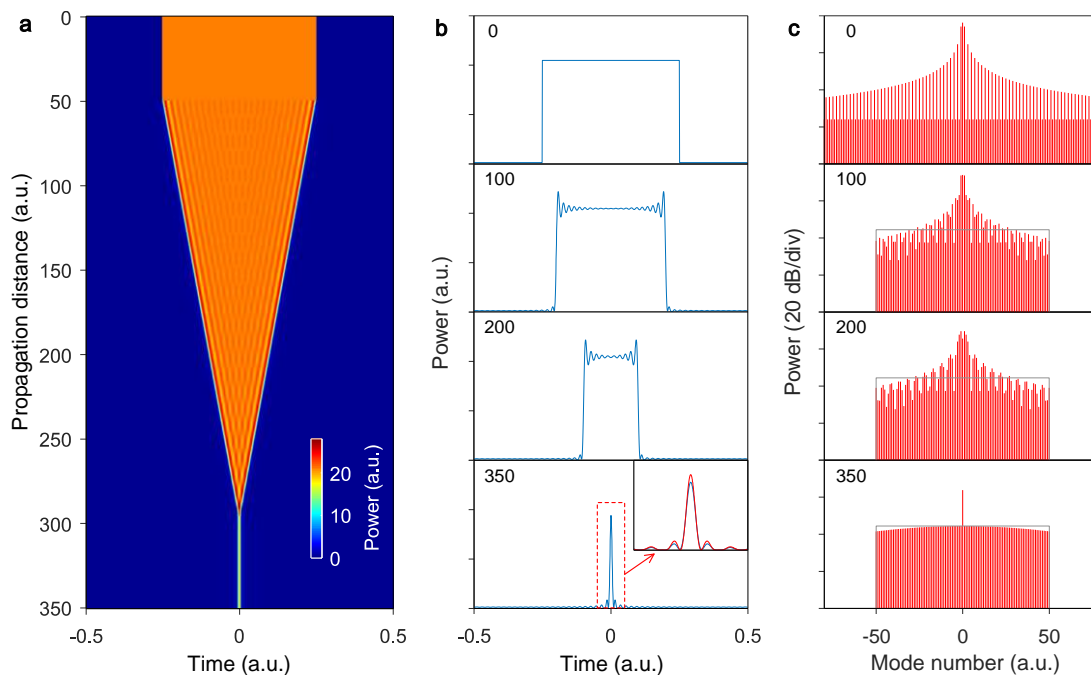


Figure 2 | Numerically simulated Nyquist soliton formation through interlocking of two switching waves. The initial field contains two steps that connect the two homogenous solutions of the nonlinear equation. **a**, Evolution of intracavity field versus propagation distance. An ideal gate spectral filter is applied from the distance of 50. **b,c**, Transient waveform and spectrum at different distances (0, 100, 200, 350) in **a**. The inset in the bottom panel of **b** shows a zoom-in comparison between the numerical result (blue) and the theoretical *sinc* pulse (red). The gate filter passband is indicated by the gray lines in **c**.

Experimental results

Fiber ring cavity with programmable dispersion and loss. To study the soliton dynamics, a fiber ring cavity consisting of highly nonlinear fiber and single-mode fiber in the communication band is built. The experimental setup is shown in Figure 3. A high-resolution spectral shaper is inserted in the cavity to compensate the group velocity dispersion and apply the amplitude filtering function [33]. A short length of Erbium-doped fiber is also added to compensate the high insertion loss of the spectral shaper [34]. A 90/10 coupler is used to inject the external pump into the cavity; and another 95/5 coupler is used as a drop port to extract the soliton for characterization. The through-port transmission measured with a low probe power is shown in the inset of Figure 3. The total cavity roundtrip length is about 54.6 m, corresponding to a free spectral range (FSR) of 3.73 MHz. The net roundtrip power loss is 16.6%, corresponding to a finesse of 36. The intracavity group velocity dispersion is carefully compensated by programming the phase of the spectral shaper; and the amplitude is programmed to be a rectangle with a bandwidth of 250 GHz. The optical resolution of the spectral shaper is around 10 GHz. The measured filter shape has a full-width-at-half-maximum (FWHM) of about 250 GHz as well as two transition bands of 10 GHz (from 3-dB to 20-dB attenuation with respect to the passband center). It should be noted that the amplitude and phase of any real practical filter are correlated by the Kramas-Kronig relation due to causality [35]. Thus the overall phase cannot be completely zero even after the fiber dispersion is precisely compensated. The amplitude and causality-related phase of the cavity roundtrip transmission are measured by an optical vector network analyzer, and the results are shown in the inset of Figure 3. Abrupt phase variations in the transition bands can be observed.

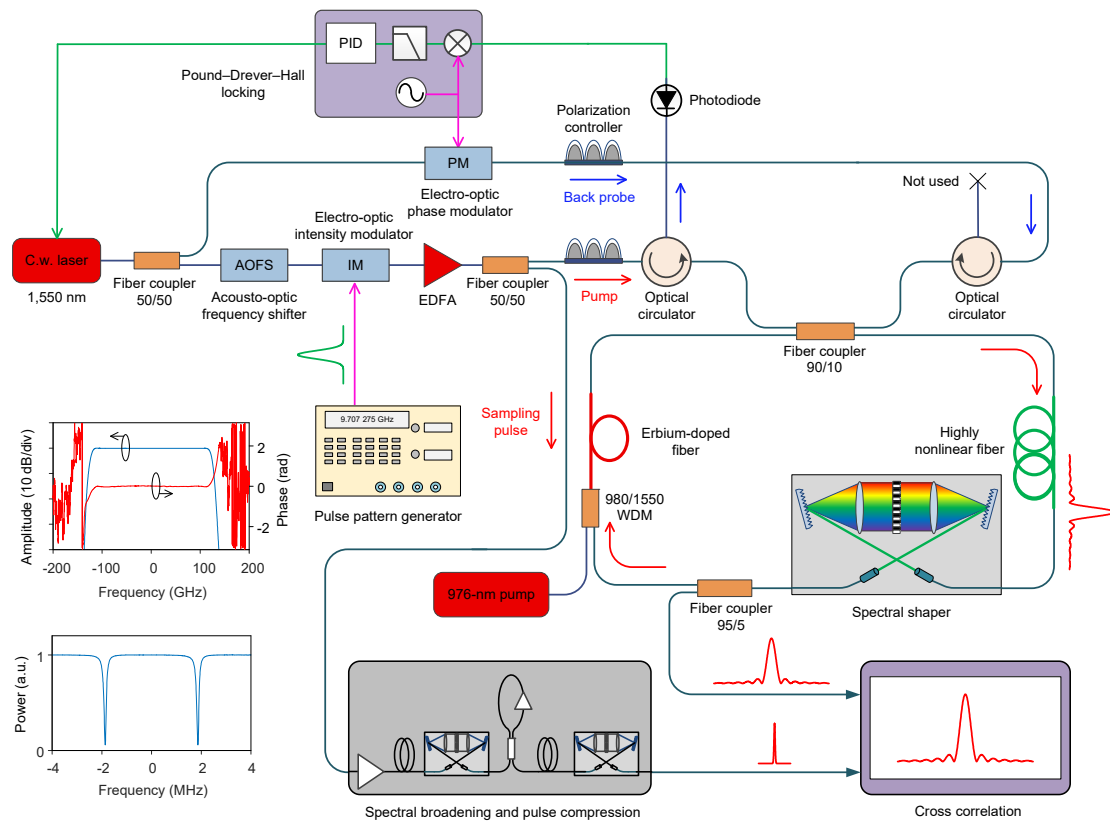


Figure 3 | Experiment setup for studying the soliton dynamics. The Kerr cavity is a fiber ring with an

embedded high-resolution spectral shaper for programmable dispersion and filter control. A short length of Erbium-doped fiber is added to partially compensate the loss. The cavity is pumped by a sub-nanosecond Gaussian pulse for soliton generation. Pound-Drever-Hall locking is used to lock the pump laser frequency to the cavity by sending a probe light in an opposite direction. On the left bottom, the upper inset shows the amplitude and phase response of the cavity roundtrip after the group velocity dispersion is compensated; the lower inset shows the measured low-power through-port transmission of the cavity. A portion of the pump pulse is spectrally broadened and compressed to a sub-picosecond pulse for measuring the soliton waveform via intensity cross correlation. EDFA: Erbium-doped fiber amplifier; WDM: wavelength-division multiplexer; PID: proportional-integral-derivative controller.

Nyquist soliton generation with pulsed pumping. To improve the pump power efficiency and avoid backward Brillouin scattering, synchronized pulsed pumping is employed to sustain the solitons [36], [37]. The pump pulse is generated by modulating a narrow-linewidth continuous-wave laser with the signals from a high-speed pulse pattern generator. The pulse shape can be well fitted by a Gaussian function with a FWHM of 87.4 ps. The peak power is boosted to 1.5 W by using an Erbium-doped fiber amplifier. The laser frequency is locked to the cavity resonance by sending a probe light through the cavity in an opposite direction and using the Pound-Drever-Hall locking technique [38]. An acousto-optic frequency shifter is employed to control the frequency detuning between the pump pulse and the cavity. To measure the soliton waveform, a high-resolution intensity cross correlation setup is built. A portion of the pump pulse is spectrally broadened and compressed to 0.2 ps, and then serves as the sampling pulse (Supplementary Section 2).

To excite solitons, the pump frequency is swept across the cavity resonance from the blue side (i.e., pump frequency higher than the resonant frequency). The measured intracavity power traces are shown in Figure 4a. Steps which usually correspond to soliton state transitions can be clearly observed. Detailed spectral and time-domain measurements show that the spectrum at each step has different number of sidelobes corresponding to different pulse width (i.e., distance between the two switching waves). The transition steps can be affected by the desynchronization between the pump pulse and the cavity. Under a proper desynchronization factor, the number of spectral sidelobes decreases one by one and the two switching waves get closer with the increase of pump detuning. The spectrum and pulse shape at some selected steps are shown in Figure 4b and 4c (see Supplementary Section 3 for more results). At the last step before the pump jumps out of the resonance, all the sidelobes disappear and a flat spectrum is obtained. The FWHM of the generated Nyquist soliton is around 4 ps. The soliton spectrum is very close to a rectangle. There are more than 66,000 lines within a 6-dB range excluding the pump, containing 99% of the total comb power.

Numerically simulated results are also shown in Figure 4. Excellent agreement is obtained between the experiment and the simulation. The causality-related phase of the spectral shaper, corresponding to non-zero higher-order dispersion, has been taken into account. It was found recently that the higher-order dispersion itself may interplay with the Kerr nonlinearity and enable soliton formation when the second-order dispersion is close to zero [29], [30]. It is thus questionable whether the soliton in our system is primarily stabilized by the higher-order dispersion or the spectral filter. Supplementary Figure S6 shows the results when the causality-

related phase is set to zero in our simulation. Quite similar Nyquist soliton can be obtained, which implies that the soliton is indeed formed by a critical balance of the dispersive loss and the Kerr nonlinearity. It is also found that one-by-one sidelobe decrement is not a prerequisite for the final Nyquist soliton generation. Sometimes the detuning region of some intermediate states may be too narrow to be observed and the sidelobes disappear by two or more.

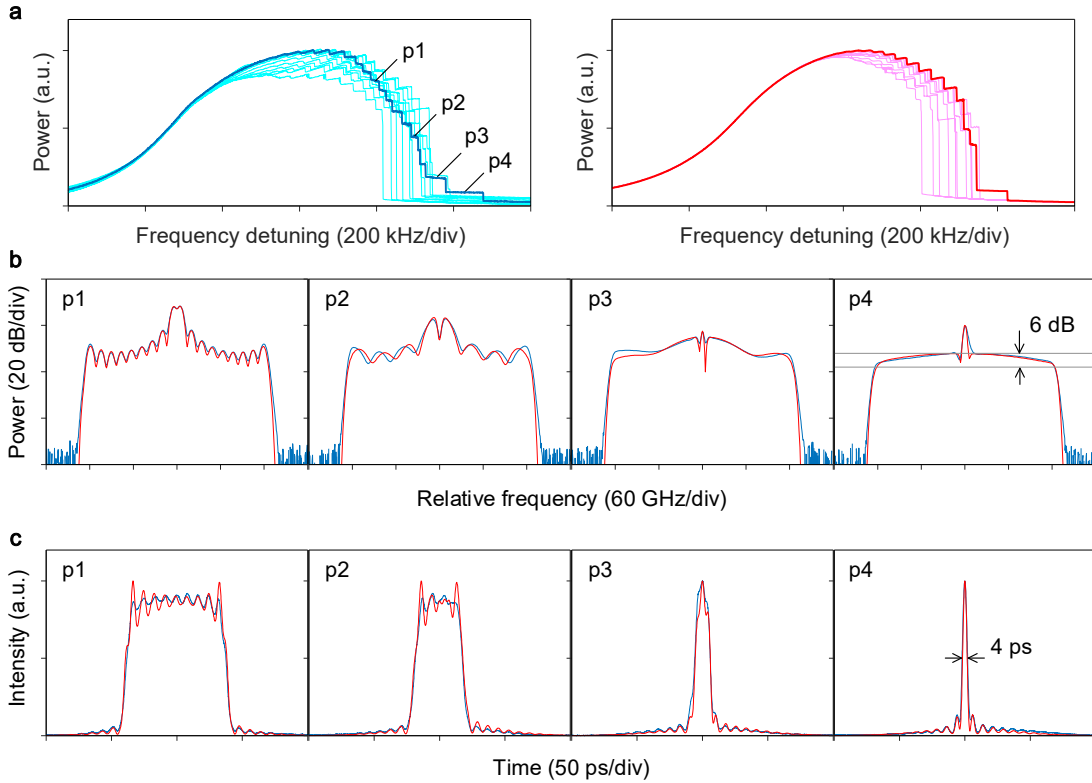


Figure 4 | Nyquist soliton transition dynamics under pulsed pumping. **a**, Intracavity power versus pump frequency detuning (left: measured; right: simulated). Multiple traces with different desynchronization between the pump pulse and the cavity are overlaid. One of them showing Nyquist soliton generation is highlighted. **b,c**, Spectrum and pulse shape at different detunings marked in **a** (blue: measured; red: simulated). The number of spectral sidelobes decreases one by one with the increase of pump detuning, corresponding to the two switching waves getting closer towards each other. A Nyquist soliton with a flat spectrum is formed at the detuning of p4. The comb lines (not visible due to the limited resolution of the spectrum analyzer) within a 6-dB range contain 99% of the total comb power excluding the pump. The full-width-at-half-maximum of the pulse is around 4 ps.

Transition between Nyquist soliton and dispersion-driven soliton. It is interesting to investigate the relation between filter-driven and dispersion-driven solitons. When the second-order dispersion is not zero in our system, both the dispersion and the spectral filter will be responsible for soliton pulse shaping. Figure 5 shows the results when different amounts of second-order dispersion are applied by programming the spectral shaper. The soliton spectrum becomes slightly flatter when the net roundtrip dispersion is slightly normal (0.63 ps^2 , corresponding to 30-m single-mode fiber with an inverted dispersion sign). However, the soliton existence region becomes narrower; and it is more difficult to get stable Nyquist solitons when the dispersion is further increased. When the net dispersion is anomalous, the spectral

intensity close to the pump gets enhanced. Two cases with a net dispersion of -1.06 ps^2 and -4.22 ps^2 (corresponding to 50-m and 200-m single-mode fiber, respectively) are shown. With the increase of dispersion, the soliton gets more like the classical soliton with a sech^2 -shaped spectral envelope [1], [15]. The ripples aside the main pulse, which is a signature of Nyquist pulse, gets diminished. A chaotic region can also be observed from the intracavity power transition trace, which is attributed to modulational instability in the anomalous dispersion region [15]. We find that the filtering effect in combination with a proper pump-cavity desynchronization can enable deterministic single soliton generation. Indeed, the inclusion of spectral filtering effect in DKS generation increases the dimensions of parameter space, bringing new and rich soliton dynamics that is worth further investigation.

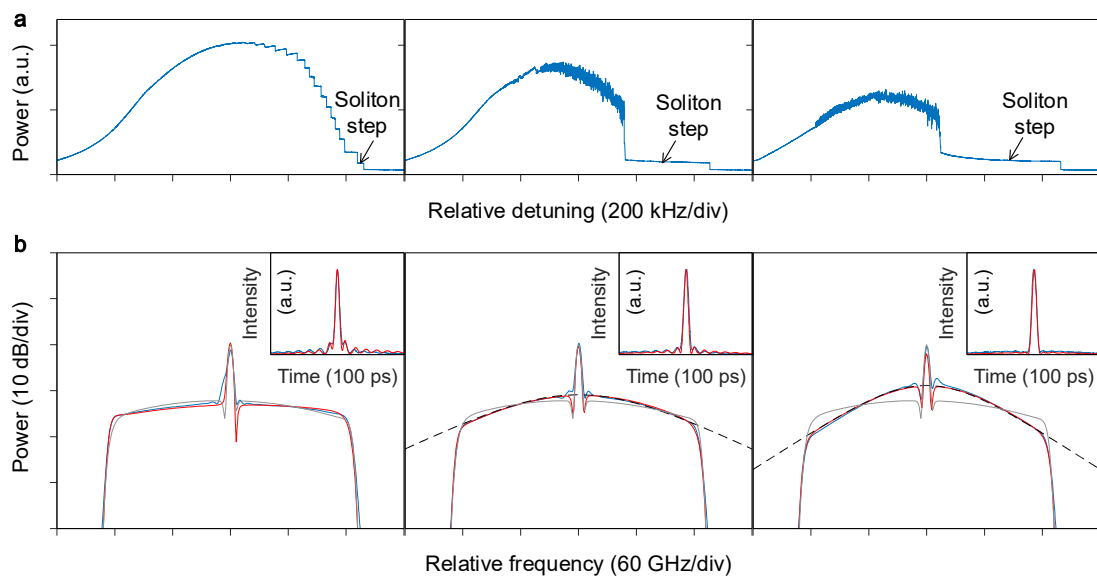


Figure 5 | Transition between filter-driven and dispersion-driven solitons. **a**, Intracavity power versus pump frequency detuning. From left to right, the net roundtrip dispersion is 0.63 ps^2 , -1.06 ps^2 , and -4.22 ps^2 , respectively. Soliton transition steps can be observed. A chaotic region with higher noise can also be observed when the dispersion is negative (anomalous). **b**, Soliton spectrum and pulse shape (inset) at the corresponding soliton steps indicated in **a** (blue: measured; red: simulated). The result with zero dispersion is also shown for comparison (gray solid line). With the increase of anomalous dispersion, the soliton gets closer to the classical dispersion-driven soliton of which the spectral envelope can be fitted by a sech^2 function (black dash line).

Discussion

In summary, DKSs enabled by a balance of pure dispersive loss and Kerr gain have been observed and investigated in a coherently driven fiber ring with programmable dispersion and loss. With gate spectral filtering and pulsed pumping, deterministic generation of Nyquist solitons with ultra-flat spectrum is demonstrated. It should be noted that, although the fiber ring in our experiment is constructed of discrete elements with alternating normal and anomalous dispersion, the observed soliton is distinct from that in stretched-pulse mode-locked lasers [39]. Supplementary Figure S6 shows the simulation results based on a precise full map of our

experimental setup. The loss (gain), nonlinearity, and dispersion of each component are considered individually in a sequence. No obvious difference is observed compared to the results based on a simplified model in which the effect of group velocity dispersion is taken into account by a net dispersion term per roundtrip (Supplementary Section 1.2).

The Nyquist soliton dynamics reported here can be directly exploited for microcomb generation with miniature microresonators. One main challenge would be tailoring the frequency-dependent loss as well as the group velocity dispersion on an integrated photonics platform. The recently reported photonic crystal microcavities seem to be a highly promising way [31]. Low-loss Fabry–Pérot resonators formed by photonic crystal reflectors can already reach a quality factor higher than 10^5 ; and Kerr comb generation has been demonstrated. Our finding shows clear evidence that dispersive loss engineering constitutes an additional powerful freedom for tailoring cavity solitons. It will be particularly useful in Kerr frequency comb generation with superior spectral qualities for specified applications.

Methods

Nyquist soliton generation and characterization. The fiber ring cavity is mainly composed of 21-m highly nonlinear fiber (YOFC NL-1550-NEG) and ~30-m single-mode fiber. A high-resolution spectral shaper (Finisar) is inserted for programmable dispersion and loss control. A 0.6-m Erbium-doped fiber (EDF, YOFC EDF13) is added to partially compensate the loss. The EDF is pumped by a 1.8-W 976-nm laser, offering a gain of ~4.1 dB. The net roundtrip power loss is 16.6%, corresponding to a cavity finesse of 36. The pump pulse is generated by modulating a continuous-wave narrow-linewidth laser (OEwaves) with the signals from a pulse pattern generator (Anritsu). An EDF amplifier is used to increase the peak power to 1.5 W. A narrow-band filter (not shown in Figure 3) is used to reject the amplified spontaneous emission noise. The pump pulse is injected to the cavity through a 90/10 coupler. A 95/5 coupler is used to extract the soliton after the spectral shaper for characterization. To maintain a stable pump-cavity frequency detuning for soliton generation, the pump laser frequency is first locked to the cavity resonance by using the Pound-Drever-Hall locking method (the probe light is sent in an opposite direction); an acousto-optic frequency shifter is then used to tune the frequency of the pump pulse. The polarizations of the probe and the pump are adjusted orthogonal to minimized their mutual interference. The soliton spectrum is measured by a commercial spectrum analyzer (Yokogawa) with a resolution of 0.02 nm. The waveform is measured by a home-built intensity cross correlator with a resolution of 0.2 ps. The synchronous sampling pulse is generated by sending a portion of the pump pulse through a spectral broadening and pulse compression stage (see Supplementary Section 2 for more details).

Numerical simulation. The results in Figure 2 are simulated based on the following normalized Lugiato–Lefever (L-L) equation including frequency-dependent loss and with zero group velocity dispersion (Supplementary Section 1.1).

$$\frac{\partial U}{\partial \xi} = \left[-1 - i\Delta - \sum_{k=1}^{\infty} \frac{\sigma_k}{k!} \left(i \frac{\partial}{\partial T} \right)^k + i|U|^2 \right] U + S$$

Here, U is the normalized field amplitude in the cavity; ξ is the propagation distance; T is the time (usually called a fast time in the literature); Δ is the pump-cavity detuning; σ_k is the dispersive loss; and S is the pump field. The equation is numerically integrated with the split-step Fourier method. The dispersive loss is applied in the frequency domain by multiplying the field spectrum with a filter. The simulation parameters are $S=10$ and $\Delta=19$. The roundtrip time is 1. The filter transfer function is an ideal rectangle containing 101 modes in the passband.

The simulation results in Figure 4 and 5 are based on a simplified model in which the effects of Kerr nonlinearity, dispersion and loss are considered respectively by lumped terms in one roundtrip (Supplementary Section 1.2). The field at the end of the $(n+1)$ th round is related to that after the n th round by

$$A_{n+1} = \sqrt{(1-\theta)(1-\alpha_L)} e^{-i(\delta_L + \gamma P_n L)} \hat{F} A_n + i\sqrt{\theta} A_p$$

where A is the field amplitude; $P = |A|^2$ is the field power; L is the roundtrip length; α_L is the universal roundtrip power loss for all the modes; δ_L is the pump-cavity phase detuning; γ is the average Kerr coefficient; θ is the pump-cavity power coupling ratio; and A_p is the pump field. The operator \hat{F} accounts for the effects that can be easily applied in the frequency domain, including the group velocity dispersion, the frequency-dependent loss, and the pump-cavity desynchronization. The simulation parameters are $\theta = 10.4\%$, $\alpha_L = 16.6\%$, $\gamma = 4.6 \times 10^{-3} \text{ m}^{-1} \text{ W}^{-1}$, and $L = 54.6 \text{ m}$. The pump pulse has a Gaussian shape with a full-width-at-half-maximum of 87.4 ps. The peak power is 1.5 W. The measured filter transfer function (shown in the inset of Figure 3) including both amplitude and phase are employed in the simulation.

Acknowledgement

The authors thank Jiachen Li for the help in measuring the transfer function of spectral shaper. This work was supported in part by the National Natural Science Foundation of China (grant numbers 61690191 and 61690192), Zhejiang Lab (2020LC0AD01), and the Open Project Program of Wuhan National Laboratory for Optoelectronics (2018WNLOKF011).

References

- [1] Leo, F. *et al.* Temporal cavity solitons in one-dimensional Kerr media as bits in an all-optical buffer. *Nature Photon.* **4**, 471-476 (2010).
- [2] Kippenberg, T. J., Gaeta, A. L., Lipson, M. & Gorodetsky, M. L. Dissipative Kerr solitons in optical microresonators. *Science* **361**, eaan8083 (2018).
- [3] Gaeta, A. L., Lipson, M. & Kippenberg, T. J. Photonic-chip-based frequency combs. *Nature Photon.* **13**, 158-169 (2019).
- [4] Stern, B., Ji, X., Okawachi, Y., Gaeta, A. L. & Lipson, M. Battery-operated integrated frequency comb generator. *Nature* **562**, 401-405 (2018).

- [5] Shen, B. *et al.* Integrated turnkey soliton microcombs. *Nature* **582**, 365-369 (2020).
- [6] Suh, M.-G., Yang, Q.-F., Yang, K. Y., Yi, X. & Vahala, K. J. Microresonator soliton dual-comb spectroscopy. *Science* **354**, 600–603 (2016).
- [7] Marin-Palomo, P. *et al.* Microresonator-based solitons for massively parallel coherent optical communications. *Nature* **546**, 274–279 (2017).
- [8] Trocha, P. *et al.* Ultrafast optical ranging using microresonator soliton frequency combs. *Science* **359**, 887–891 (2018).
- [9] Suh, M.-G. & Vahala, K. J. Soliton microcomb range measurement. *Science* **359**, 884–887 (2018).
- [10] Spencer, D. T. *et al.* An optical-frequency synthesizer using integrated photonics. *Nature* **557**, 81–85 (2018).
- [11] Feldmann, J. *et al.* Parallel convolutional processing using an integrated photonic tensor core. *Nature* **589**, 52-58 (2021).
- [12] Wu, J. *et al.* 11 TOPS photonic convolutional accelerator for optical neural networks. *Nature* **589**, 44-51 (2021).
- [13] Xue, X. *et al.* Microcomb-based true-time-delay network for microwave beamforming with arbitrary beam pattern control. *J. Light. Technol.* **36**, 2312-2321 (2018).
- [14] Wu, J. *et al.* RF photonics: An optical micro-combs' perspective. *J. Sel. Top. Quantum Electron.* **24**, 6101020 (2018).
- [15] Herr, T. *et al.* Temporal solitons in optical microresonators. *Nature Photon.* **8**, 145-152 (2014).
- [16] Xue, X. *et al.* Mode-locked dark pulse Kerr combs in normal-dispersion microresonators. *Nature Photon.* **9**, 594–600 (2015).
- [17] Lobanov, V. E., Lihachev, G., Kippenberg, T. J. & Gorodetsky, M. L. Frequency combs and platons in optical microresonators with normal GVD. *Opt. Express* **23**, 7713-7721 (2015).
- [18] Brasch, V. *et al.* Photonic chip-based optical frequency comb using soliton Cherenkov radiation. *Science* **351**, 357-360 (2016).
- [19] Xue, X. *et al.* Normal-dispersion microcombs enabled by controllable mode interactions. *Laser Photon. Rev.* **9**, L23-L28 (2015).
- [20] Helgason, Ó. B. *et al.* Dissipative solitons in photonic molecules. *Nature Photon.* **15**, 305-310 (2021).
- [21] Perego, A. M., Turitsyn, S. K. & Staliunas, K. Gain through losses in nonlinear optics. *Light Sci. Appl.* **7**, 43 (2018).
- [22] Bessin, F. *et al.* Gain-through-filtering enables tunable frequency comb generation in passive optical resonators. *Nature Comm.* **10**, 4489 (2019).
- [23] Huang, S. W. *et al.* Mode-locked ultrashort pulse generation from on-chip normal dispersion microresonators. *Phys. Rev. Lett.* **114**, 053901 (2015).
- [24] Spiess, C. *et al.* Chirped temporal solitons in driven optical resonators. arXiv:1906.12127.
- [25] Soto, M. A. *et al.* Optical sinc-shaped Nyquist pulses of exceptional quality. *Nature Comm.* **4**, 2898 (2013).
- [26] Nakazawa, M., Yoshida, M. & Hirooka, T. The Nyquist laser. *Optica* **1**, 15-22 (2014).
- [27] Boscolo, S., Finot, C. & Turitsyn, S. K. Bandwidth programmable optical Nyquist pulse generation in passively mode-locked fiber laser. *IEEE Photon. J.* **7**, 7802008 (2015).
- [28] Nakazawa, M. & Hirooka, T. A non-perturbative mode-locking theory of the Nyquist laser with a Dirichlet kernel solution. *IEEE J. Quantum Electron.* **52**, 1300113 (2016).
- [29] Anderson, M. H., Lihachev, G., Weng, W., Liu, J. & Kippenberg, T. J. Zero-dispersion Kerr solitons in optical microresonators. arXiv:2007.14507.

- [30] Li, Z., Xu, Y., Coen, S., Murdoch, S. G. & Erkintalo, M. Experimental observations of bright dissipative cavity solitons and their collapsed snaking in a Kerr resonator with normal dispersion driving. *Optica* **7**, 1195-1203 (2020).
- [31] Yu S., Jung, H., Briles, T. C., Srinivasan, K. & Papp S. B. Photonic-crystal-reflector nanoresonators for Kerr-frequency combs. *ACS Photon.* **6**, 2083-2089 (2019).
- [32] Garbin, B. *et al.* Dissipative polarization domain walls in a passive coherently driven Kerr resonator. *Phys. Rev. Lett.* **126**, 023904 (2021).
- [33] Weiner, A. M. Femtosecond pulse shaping using spatial light modulators. *Rev. Sci. Instrum.* **71**, 1929-1960 (2000).
- [34] Engleburt, N., Gorza, S.-P. & Leo, F. Temporal solitons in a coherently driven active resonator. arXiv:2007.15630v1.
- [35] Toll, J. S. Causality and the dispersion relation: logical foundations. *Phys. Rev.* **104**, 1760-1770 (1956).
- [36] Anderson, M., Leo, F., Coen, S., Erkintalo, M. & Murdoch, S. G. Observations of spatiotemporal instabilities of temporal cavity solitons. *Optica* **3**, 1071-1074 (2016).
- [37] Obrzud, E., Lecomte, S. & Herr T. Temporal solitons in microresonators driven by optical pulses. *Nature Photon.* **11**, 600-607 (2017).
- [38] Eric D. Black. An introduction to Pound–Drever–Hall laser frequency stabilization. *Am. J. Phys.* **69**, 79-87 (2001).
- [39] Grelu, P. & Akhmediev, N. Dissipative solitons for mode-locked lasers. *Nature Photon.* **6**, 84-92 (2012).

Supplementary information to The Nyquist soliton Kerr comb

Xiaoxiao Xue¹, Bofan Yang, Mian Wang, Shangyuan Li, Xiaoping Zheng², and Bingkun Zhou

Department of Electronic Engineering, Beijing National Research Center for Information Science and Technology, Tsinghua University, Beijing 100084, China

¹xuexx@tsinghua.edu.cn; ²xpzheng@tsinghua.edu.cn

1. Theoretical model and numerical simulation

1.1 Continuous-wave pumped equation

When the Kerr cavity is pumped by a continuous wave, the mean-field Lugiato–Lefever (L-L) equation including all orders of dispersion and frequency-dependent loss is given by

$$\frac{\partial A}{\partial z} = \left[-\alpha_0 - i\delta_0 + i \sum_{k=2}^{\infty} \frac{\beta_k}{k!} \left(i \frac{\partial}{\partial \tau} \right)^k - \sum_{k=1}^{\infty} \frac{\alpha_k}{k!} \left(i \frac{\partial}{\partial \tau} \right)^k + i\gamma |A|^2 \right] A + \kappa A_p. \quad (\text{S1})$$

Here, A is the field amplitude; z is the propagation distance; τ is the time; α_0 is the universal amplitude loss per unit length; δ_0 is the pump-cavity detuning given by $\delta_0 = (\omega_0 - \omega_p)T_R/L$ where ω_p and ω_0 are the angular frequency of the pump and the cavity, respectively; T_R and L are the roundtrip time and length, respectively; β_k is the different orders of dispersion; α_k is the frequency-dependent loss; γ is the nonlinear coefficient; κ is the pump-cavity coupling rate; A_p is the pump field amplitude.

When the group velocity dispersion is zero, the equation becomes

$$\frac{\partial A}{\partial z} = \left[-\alpha_0 - i\delta_0 - \sum_{k=1}^{\infty} \frac{\alpha_k}{k!} \left(i \frac{\partial}{\partial \tau} \right)^k + i\gamma |A|^2 \right] A + \kappa A_p \quad (\text{S2})$$

with a normalized form given by

$$\frac{\partial U}{\partial \xi} = \left[-1 - i\Delta - \sum_{k=1}^{\infty} \frac{\sigma_k}{k!} \left(i \frac{\partial}{\partial T} \right)^k + i|U|^2 \right] U + S. \quad (\text{S3})$$

The normalization is performed as follows

$$\begin{aligned} U &= A \sqrt{\frac{\gamma}{\alpha_0}}; & \xi &= \alpha_0 z; \\ T &= \frac{\tau}{T_R}; & \Delta &= \frac{\delta_0}{\alpha_0}; \\ \sigma_k &= \frac{\alpha_k}{\alpha_0 T_R^k}; & S &= \frac{\kappa A_p}{\alpha_0} \sqrt{\frac{\gamma}{\alpha_0}}; \end{aligned}$$

where T_R is the cavity roundtrip time. The simulation presented in Figure 2 of the main paper is performed based on Equation (S3) with $S = 10$ and $\Delta = 19$. The normalized roundtrip time is 1. The initial field contains two steps that connect the two homogeneous solutions of the equation, given by

$$U(T=0) = \begin{cases} U_u, & -0.25 \leq T \leq 0.25 \\ U_l, & -0.5 \leq T < -0.25, 0.25 < T \leq 0.5 \end{cases} \quad (\text{S4})$$

where U_u and U_l are given by

$$U_{u,l} = \frac{iS}{1+i(\Delta - P_{u,l})}; \quad (\text{S5})$$

and $P_{u,l} = |U_{u,l}|^2$ represents the upper and lower steady-state solutions of

$$P^3 - 2\Delta P^2 + (1 + \Delta^2)P = |S|^2. \quad (\text{S6})$$

The frequency-dependent loss is applied in the frequency domain by multiplying the field spectrum with a filter. The filter transfer function is an ideal rectangle containing 101 modes in the passband, given by

$$H(N) = \begin{cases} 1, & -50 \leq N \leq 50 \\ 0, & \text{others} \end{cases} \quad (\text{S7})$$

where N is the relative mode number with $N = 0$ representing the pump mode.

1.2 Pulse pumped equation

When the Kerr cavity is pulse pumped, the L-L equation can be written as

$$\frac{\partial A}{\partial z} = \left[-\alpha_0 - i\delta_0 - \eta \frac{\partial}{\partial \tau} + i \sum_{k=2}^{\infty} \frac{\beta_k}{k!} \left(i \frac{\partial}{\partial \tau} \right)^k - \sum_{k=1}^{\infty} \frac{\alpha_k}{k!} \left(i \frac{\partial}{\partial \tau} \right)^k + i\gamma |A|^2 \right] A + \kappa A_p \quad (\text{S8})$$

An additional term with the parameter η is included to account for the desynchronization between the pump pulse rate R_p and the cavity free spectral range R_c . If we define a desynchronization factor $d = (R_p - R_c)/R_c$, then $\eta = d/[R_c L(1+d)]$.

For the simulation presented in Figure 4 and 5 of the main paper, the integration step size is one roundtrip and a simplified model is employed in which the dispersion, pump coupling, propagation loss, and Kerr nonlinearity are represented respectively by lumped terms. The field at the end of the $(n+1)$ th round is related to the n th round by

$$A_{n+1} = \sqrt{(1-\theta)(1-\alpha_L)} e^{-i(\delta_L + \gamma P_n L)} \hat{F} A_n + i\sqrt{\theta} A_p \quad (\text{S9})$$

where θ is the power coupling ratio of the pump coupler, related to κ by $\theta = \kappa^2 L^2$; α_L is the roundtrip power loss, related to α_0 by $\alpha_L = 1 - e^{-2\alpha_0 L}$; $\delta_L = (\omega_0 - \omega_p)T_R$ is the pump-

cavity phase detuning per roundtrip; γ is the average Kerr coefficient given by $\gamma = (\gamma_{\text{HNLF}}L_{\text{HNLF}} + \gamma_{\text{SMF}}L_{\text{SMF}})/L$ where γ_{HNLF} and γ_{SMF} represent the Kerr coefficient of the highly nonlinear fiber and the single-mode fiber; L_{HNLF} and L_{SMF} are the length; $P_n = |A_n|^2$ is the field power. The operator \hat{F} accounts for the effects that can be easily applied in the frequency domain, including the group velocity dispersion, the frequency dependent loss, and the pump-cavity desynchronization. The simulation parameters are $\theta = 10.4\%$, $\alpha_L = 16.6\%$, $\gamma = 4.6 \times 10^{-3} \text{ m}^{-1}\text{W}^{-1}$, and $L = 54.6 \text{ m}$. The pump pulse has a Gaussian shape with a full-width-at-half-maximum (FWHM) of 87.4 ps. The peak power is 1.5 W. The measured filter transfer function (shown in the inset of Figure 3) including both amplitude and phase are employed in the simulation. Nyquist solitons can be obtained when the pump-cavity desynchronization $\eta = -7.88 \times 10^{-16} \text{ s/m}$.

1.3 Estimated Nyquist soliton waveform

For the normalized Eq. (S3), the bright Nyquist soliton can be estimated by an ideal *sinc* pulse sitting atop the lower steady-state continuous-wave background, given by

$$U_b = U_1 + (U_u - U_1) \frac{\sin \pi B_f T}{\pi B_f T} \quad (\text{S10})$$

where B_f is the bandwidth of the gate bandpass filter.

When the soliton is a dark pulse as is shown in the next section, the estimation is a negative *sinc* pulse embedded in the upper steady-state continuous-wave background, given by

$$U_d = U_u - (U_u - U_1) \frac{\sin \pi B_f T}{\pi B_f T} \quad (\text{S11})$$

1.4 Dark Nyquist soliton

Figure S1 shows a simulated example in which two switching waves are interlocked to form a dark Nyquist pulse. The simulation is based on Eq. (S3) with $S = 10$ and $\Delta = 11.5$. The initial field contains two steps that connect the two homogeneous solutions of the equation. A gate spectral filter with a bandwidth of 101 modes is applied from the propagation distance of 50. The high plateau expands with the movement of the switching waves. A stable dark pulse is formed after the distance of 300. The transient waveform and spectrum are shown in Figure S1b and S1c. The estimated *sinc* pulse given by Eq. (S11) is also shown (red) in the bottom panel of Figure S1b for comparison. Compared to the bright soliton in Figure 2 of the main paper, the spectrum of the dark soliton has a slightly increased power variation (7.2 dB) within the filter passband.

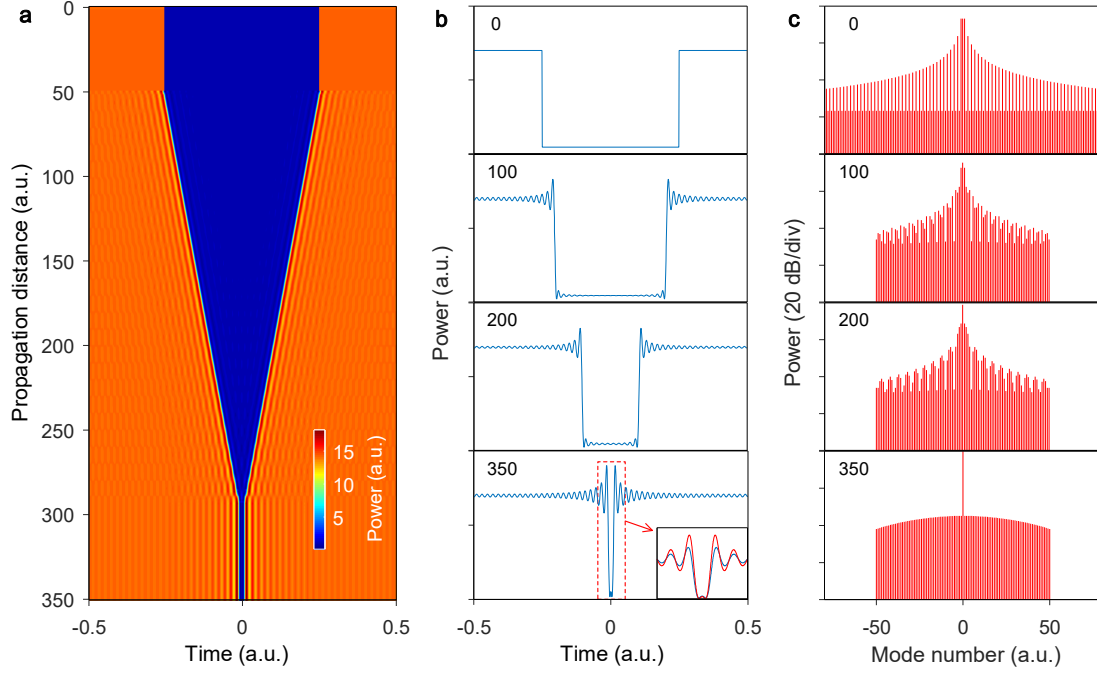


Figure S1 | Dark Nyquist soliton formation. **a**, Evolution of intracavity field versus propagation distance. **b,c**, Transient waveform and spectrum at the distances of 0, 100, 200, and 350. The theoretical *sinc* pulse (red) is shown in the bottom panel of **b** for comparison.

1.5 Soliton hysteresis

Figure S2 shows an example of soliton hysteresis. In Figure S2a, two traces of intracavity power versus pump detuning are shown. The pump power is kept 100 (i.e., $|S|^2 = 100$). For the higher branch, a dark soliton is first obtained at point d1 ($\Delta = 11.5$) following the procedure in Figure S1; the detuning is then gradually changed with small steps in the forward (increasing) and backward (decreasing) directions. At each detuning step, the equation is numerically integrated until the field reaches a stable state. When the detuning is larger than 17.16, the switching waves forming the dark soliton depart and move in an opposite direction. The field switches to a bright soliton when the switching waves get interlocked again. For the lower branch, a bright soliton is first obtained at point b3 ($\Delta = 19$) following the procedure in Figure 2 of the main paper; and the detuning is then scanned. The field switches to a dark soliton when the detuning is lower than 12.03. The soliton area is marked in pink. A detuning region where both bright and dark solitons coexist can be clearly observed. The soliton waveforms at the points indicated in Figure S2a are shown in Figure S2b and S2c.

Figure S2d shows the intracavity power versus the pump power when the detuning is kept 19 ($\Delta = 19$). For the lower branch, a bright soliton is first obtained at point b3 ($|S|^2 = 100$) following the procedure in Figure 2 of the main paper; and the pump power is then scanned. For the higher branch, a dark soliton is first obtained at point d6 ($|S|^2 = 350$) and the pump power is then scanned. The soliton waveforms are shown in Figure S2e and S2f.

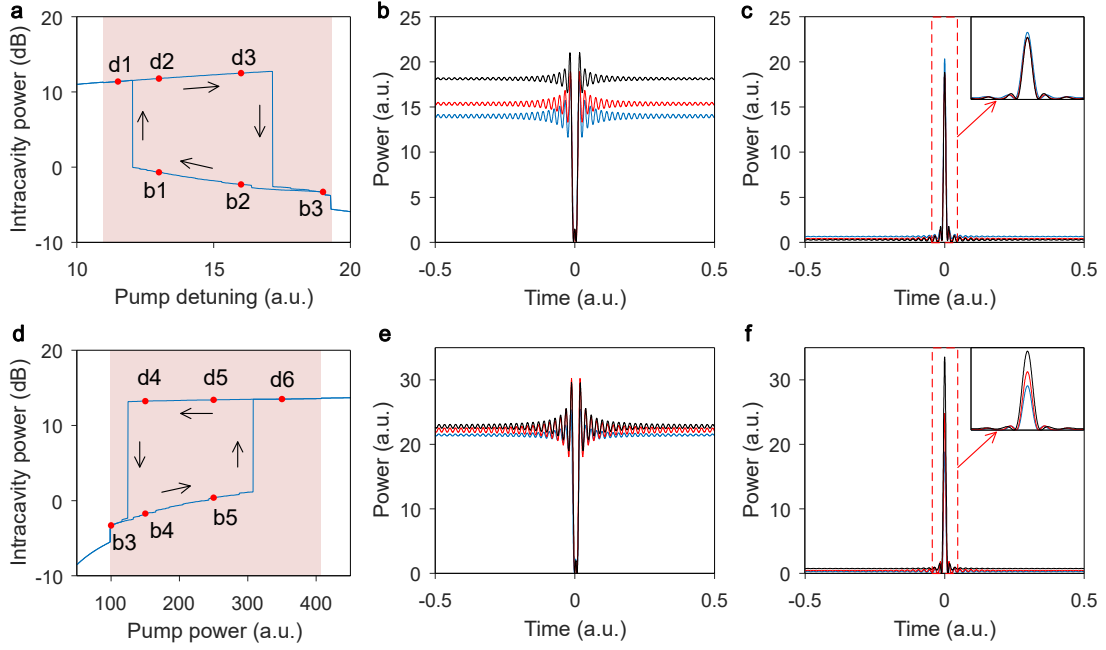


Figure S2 | Soliton hysteresis. **a,d**, Intracavity power versus pump detuning (when $S = 10$) and power (when $\Delta = 19$). The soliton existence region is marked in pink. **b**, Dark solitons at points d1 (blue), d2 (red), and d3 (black) indicated in **a**. **c**, Bright solitons at points b1 (blue), b2 (red), and b3 (black) indicated in **a**. **e**, Dark solitons at points d4 (blue), d5 (red), and d6 (black) indicated in **d**. **f**, Bright solitons at points b3 (blue), b4 (red), and b5 (black) indicated in **d**.

1.6 Solitons with Gaussian filter

Figure S3 shows the results when the filter shape is a Gaussian function given by

$$H(N) = e^{-2N/B_G|^n} \quad (\text{S12})$$

where $B_G = 101$ is the bandwidth and n is the order. The simulation parameters are $S = 10$ and $\Delta = 15$. The soliton waveform with $n = 2, 5$, and 20 is shown in Figure S3a-S3c, respectively. The spectrum is shown in Figure S3d-S3f. When the filter gets close to a rectangle, the soliton gets more like a Nyquist pulse.

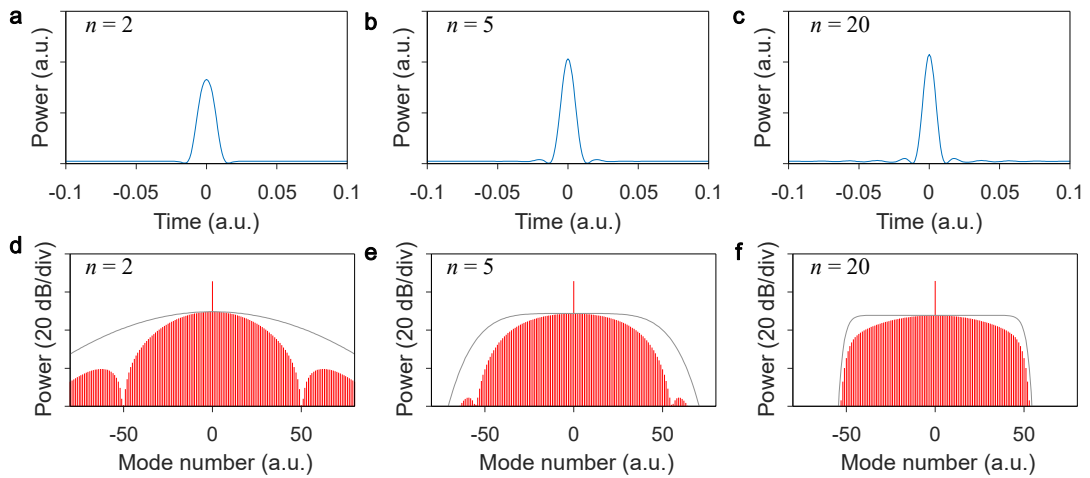


Figure S3 | Solitons with Gaussian filter. **a,b,c**, Soliton waveform. **d,e,f**, Comb spectrum. The filter shape is indicated by gray lines.

2. Soliton characterization with intensity cross correlation

The intensity cross correlation setup for measuring the soliton pulse shape is shown in Figure S4. The synchronous sampling pulse is generated through a multiple-stage spectral broadening and pulse compression procedure. A portion of the Gaussian pump pulse is first amplified to a peak power of ~ 200 W, and sent through a 50-m highly nonlinear fiber (HNLf). The spectrum is broadened to ~ 2 nm and the pulse is compressed by a spectral shaper. A nonlinear amplifying loop mirror (NALM) composed of 2-m HNLf and 0.5-m Erbium-doped fiber (LIEKKI Er-110) is used to improve the pulse quality and further broaden the spectrum to ~ 6 nm. After passing through another 50-m HNLf, the spectral bandwidth exceeds 100 nm. A second spectral shaper is used to select the spectrum between 1527-1567 nm and shape the pulse to a Gaussian function with a FWHM of 0.2 ps. The peak power of the output pulse is ~ 130 W. The pulse is much narrower than the Nyquist soliton to be measured (4 ps), making it possible to capture the fine temporal features with a high resolution.

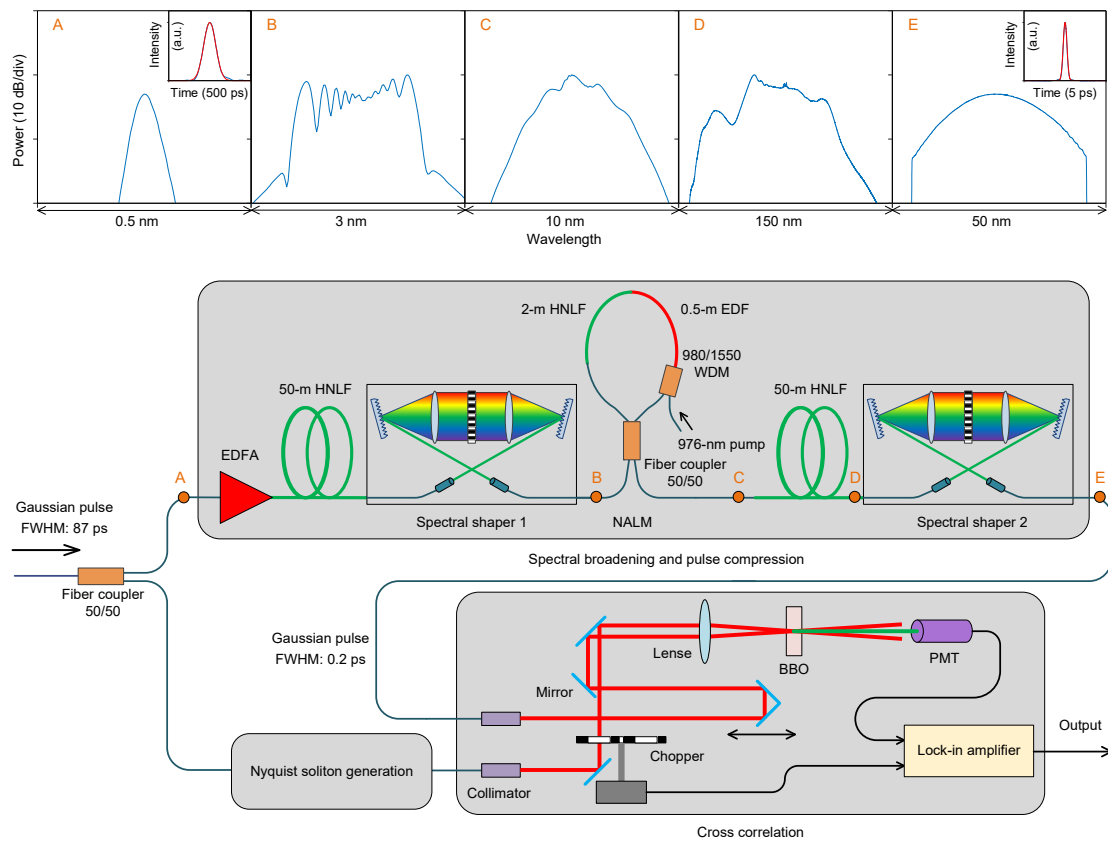


Figure S4 | Intensity cross correlator for soliton characterization. The insets on top show the spectra at different locations (A, B, C, D, E). The pump pulse waveform at point A detected by a high-speed photodiode and the autocorrelation of the compressed Gaussian pulse at point E are also shown (blue: measured; red: calculated). FWHM: full-width-at-half-maximum; EDFA: Erbium-doped fiber amplifier; HNLf: highly nonlinear fiber; EDF: Erbium-doped fiber; WDM: wavelength-division-multiplexed coupler; NALM: nonlinear amplifying loop mirror; BBO: beta barium borate crystal; PMT: photomultiplier tube.

3. Nyquist soliton transition with pulsed pumping

Figure S5 shows the full data of the soliton transition in Figure 4 of the main paper. At the step marked with p1, the spectrum contains one mainlobe and 14 sidelobes (only the sidelobes on one side are counted because of the symmetry). From p1 to p15, with the increase of pump detuning, the number of sidelobes decreases one by one. At p15, all the sidelobes disappear and only the mainlobe remains. When the detuning is further increased to p16, the mainlobe also vanishes, resulting in a flat spectrum. The measured pulse width decreases from 126 ps to 4 ps when the detuning is changed from p1 to p16. A narrow Nyquist pulse is finally obtained.

4. Effect of higher-order dispersion

The causality-related phase of the spectral shaper, corresponding to non-zero higher-order dispersion, is not crucial for soliton formation in our system. Figure S6 shows a comparison between the Nyquist solitons with and without the causality-related phase, simulated based on the simplified model described in Supplementary Section 1.2. The difference is hardly visible. The result simulated based on a full map of the fiber ring is also presented, which is also very close to that of the simplified model.

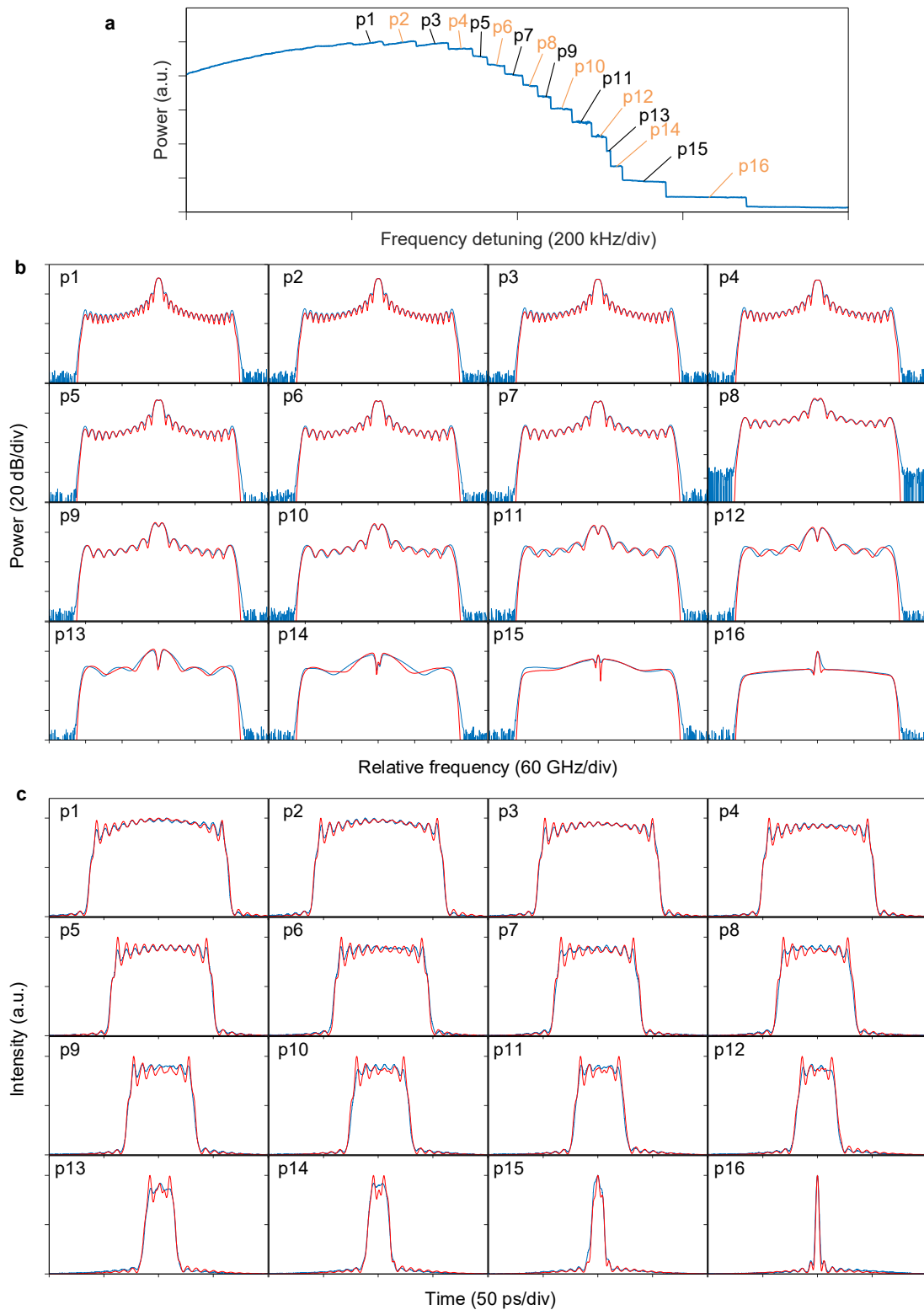


Figure S5 | Nyquist soliton transition under pulsed pumping. **a**, Intracavity power versus pump detuning. **b,c**, spectrum and pulse shape at the different steps marked in **a** (p1 to p16). Blue: measured; red: simulated.

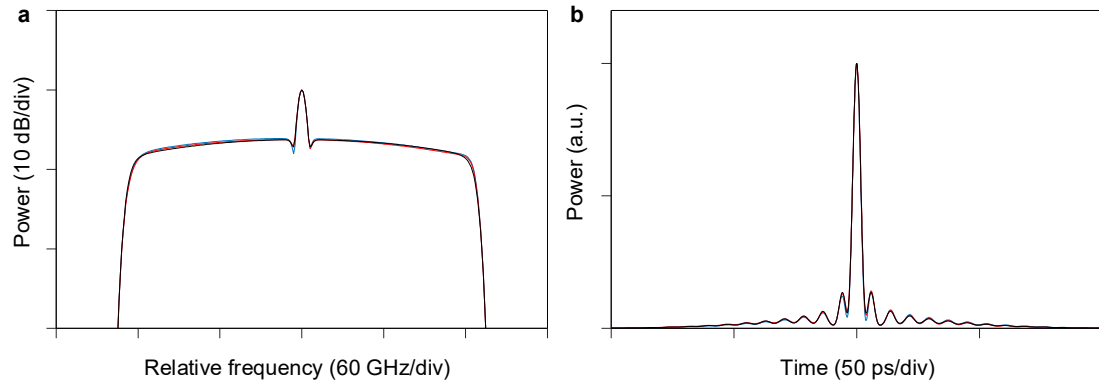


Figure S6 | Simulated Nyquist solitons based on the simplified model with (blue) and without (red) higher-order dispersion. The result based on a full-map model is also shown (black). **a**, Spectrum; **b**, Pulse shape.